Simulating Tropical Cyclone over the South-west Indian Ocean with MPAS: Sensitivity to cloud microphysics schemes

Semester Project

Name: Brian KYANJO

Semester: Fall-2021

Supervisor: Prof. Lejo Flores

Date: November 30, 2021

---

1   Introduction

Tropical cyclones (TCs), one of the strongest atmospheric features, are known for massive destruction of properties and human lifes, because they are associated with strong winds, heavy rains, and storm surges [TROPICAL CYCLONES]. Since the beginning of the 20th century, TCs have affected more than 629 million people and killed more than 1.33 million people in the tropics [Doocy et al., 2013]. TCs, which usually form over warm tropical oceans ($\geq 26°C$), are warm-core low-pressure systems with 100 - 1000 km diameter. Once established, TCs sustain their strength by absorbing warm moisture as they continue to enlarge and will last as long as the atmospheric and oceanic conditions remain favourable over the ocean. After making a landfall, TCs can last for seven days and cause severe damages as they move inland or along the coastline [Doocy et al., 2013]. The TCs that form over the Southwest Indian Ocean (SWIO) are a threat to the neighbouring countries, but Madagascar, Mauritius and La Reunion experience the most devastating and destructive impacts of the TCs, followed by the extensive coastline and the borders of Zimbabwe and Mozambique [Tropical cyclones in the South West Indian Ocean]. For instance, in 2017, Tropical Cyclone Dineo (name of a tropical cyclone), which formed on 13th February and made a landfall over Mozambique on 15th February [Moses and Ramotonto, 2018]. Dineo produced heavy rains (> 200mm day-1) and damaging winds in Inhambane (southern province in Mozambique) and destroyed around 20000 homes, directly affected about 130,000 people, and killed seven people. Its widespread torrential rains and the associated storm surge produced massive floods that killed about 271 people and caused damages that exceeded $ 200 million in Zimbabwe (USD 2017) [Cyclone Dineo. , 2020, 3 15]. Although Dineo weakened on February 17th, its remnant low still triggered heavy rainfall with flooding in Botswana. The flooding destroyed 650 households and public infrastructures (e.g. bridges, hospitals, schools, and fields), leaving hundreds of people homeless and poor (especially the low-income earners) [Moses and Ramotonto, 2018]. A month after the landfall, the impacts of Dineo landfall induced an outbreak of chlorella that infected 1,200 people and killed 2 people in Mozambique and Malawi [Cyclone Dineo. , 2020, 3 15]. Despite the devastating impacts TCs over the region, from our best knowledge, there are still no reliable systems for providing early warning on TC occurrences over region. Hence, there is a need for more studies on how to improve simulation and prediction of TC characteristics over the SWIO. This will help reduce the devastating impacts of TCs in the region.

1.1   Problem Statement

Model for Prediction Across Scales (MPAS) cloud microphysics schemes: Weather Research Forecast (WRF)-Single-Moment-Microphysics Class 6 (WSM6) and Thompson, have a significant influence in the simulation of TC; however, according to past research, the capability of these two microphysics schemes in simulating TCs over the SWIO have not been tested yet. So comparing and analysing the influence of these microphysics schemes during simulations would help us to understand which scheme is best to use and under which available conditions. This will improve predictions of TCs over the basin and will reduce on the devastating damages caused by TCs ahead of time.

1.2   Aim and objectives

This project aims to evaluate the capability of MPAS in simulating TC Dineo and examine the sensitivity of TC Dineo to two prominent cloud microphysics schemes: WSM6 and Thompson over the SWIO basin.

The three specific objectives are:

- To describe the characteristics of TC Dineo.

- To evaluate how MPAS simulates TC Dineo over the SWIO basin.

- To compare the sensitivity of WSM6 and Thompson in the simulation of TC Dineo over the SWIO basin.

2   Model Description

MPAS models use centroidal Voronic tessellations in their horizontal meshes, which provide a common software framework that gives an infrastructure for producing parallel execution, input, output, high-level driver program and other software infrastructure. The supported important features of MPAS - Atmosphere (MPAS-A) include fully-compressible, non-hydrostatic dynamics, split-explicit Runge-Kunta time integration, Exact conservation of dry-air mass and scalar, Positive-definite and monotonic transport options, Generalised terrain-following hight coordinate. Unstructured variable-resolution (horizontal) mesh integrations for the sphere and Cartesian planes is also a supported vital feature of MPAS-A [ucar, n.d.].

Version 6.0 of MPA-A consists of parameterizations of physical processes that are taken from the WRF Model. Explicitly Parameterizations of physical processes supported by MPAS-A include Radiation, Land-surface, Surface-layer, Boundary-layer, Convection, Cloud microphysics [ucar, n.d.].

MPAS-A consists of two main components, i.e., the model and initialization, built as cores within the MPAS software framework. Both the model and initialization make use of software infrastructure and the same driver program but they are compiled as separate executables. The model component consists of physics and atmospheric dynamics. The initialisation component consists of components for creating initial conditions for the atmospheric and land-surface state and updating files for the sea-surface temperature (SST) and sea ice [ucar, n.d.]. Figure. 1 shows model components within the MPAS framework. As shown in the Figure. 1 the init_atmosphere (on the left) and atmosphere (on the right) are built as separate cores within the framework (MPAS superstructure). Both cores are symbolically linked to the MPAS common infrastructure (at the bottom).
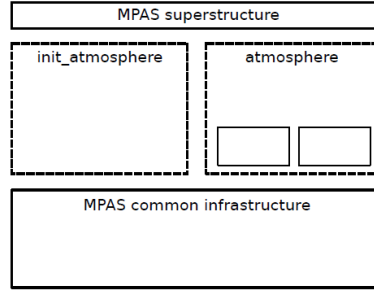

Figure 1: The initialization and model components [ucar, n.d.]

2.1   Literature Review

Several studies have shown that MPAS is one of the atmospheric models that have great potential for providing reliable early warning information on TC occurrence and characteristics over the SWIO. Furthermore, MPAS has been frequently used to simulate different atmospheric features and processes, including real-time weather, seasonal forecasting of tropical cyclones, tornadoes, and convection [ncar.ucar.edu. , n.d.]. For instance, Hashimoto et al. [2016] used MPAS to reproduce the frequency and locations of North Atlantic TCs using mesh refinement over the North Atlantic ocean. They show that MPAS simulations perform better than the Weather Research and Forecasting System (WRF) simulation because the smooth transitions between two grid resolutions in MPAS (i.e., variable mesh grid) helps the model to simulate smoother and more realistic mid-level jet structures and seasonal cloud patterns than the WRF simulations, which is influenced nested boundary condition problems. Harris and Lin [2014] also show that MPAS performs better than the High Resolution Model (HiRAM) in simulating the frequency of TCs. Although HiRAM can run at high resolution, it ignores computation of vertical acceleration, and its representation of thunderstorms and convection are still small compared to those in observation and MPAS simulations. However, despite the great potential of MPAS in simulating TCs, no studies have investigated its capability in simulating tropical cyclones over the SWIO.

2.2   Dynamic core and physics of MPAS

The effect of physical processes on state variable evolution is modelled or represented using a generic term called Model physics. The effect of these processes is observed either when these processes like radiation, phases of changes of water species are not contained in the Navier-stokes equations or when convective cells within coarse spatial resolution simulations are not resolved on the model mesh. Processes not to be resolved on the model mesh is caused by the failure of the structures to be represented on the mesh ($L < 2\Delta x$), where L is the length of the grid and Δx grid spacing. Inaccurate representation of present structures on the mesh in the dynamics below the effective resolution also causes physical processes not to be resolved on the model mesh. The physics

operates on cell-centered variables. The radial-basis-functions reconstruction and cell-edge normal velocities are used to compute the global mesh and the components of cell-centered velocity [Atmospheric physics].

The Physics in MPAS is divided into several parameterisations: microphysics, surface-layer, land-surface, short wave radiation, long wave radiation, boundary layer, convection, gravity wave drag by orography, and cloud fraction for radiation. Each parameterisation consists of different schemes for example, WSM6, Thompson and Kessler schemes are contained in microphysics, Noah is the only scheme in land-surface whereas Tiedtke, New Tiedtke, Kain-Fritsch, and Grell-Freitas are schemes in convection parameterization etc.

Successful simulations of TCs with any atmospheric model depend on how well microphysics processes are represented in the model. Microphysics contains resolved water vapour, cloud, and precipitation formation processes [Skamarock, 2008]. For this study's case, the capability of the two microphysics schemes: WSM6 and Thompson in the simulation of TC Dineo over the SWIO basin are compared. The selection of these two microphysics schemes is based on the fact that WSM6 is a default scheme in microphysics and has to be compared with either Kessler or Thompson. Thompson is selected over Kessler because it is uniquely coupled with the rapid radiative transfer model for general circulation models (RRTMG) radiation scheme and also has a unique cooperation with other parameterizations in the same physics suit. Therefore, it provides consistent information about cloud droplet size distributions during modelling. This makes WSM6 and Thompson the two prominent microphysics schemes to be used in MPAS during the entire simulations.

2.2.1 WSM6

WSM6 is developed by including graupel (q_g) to the Weather Research and Forecasting System (WRF)-Single-Moment-Microphysics Class 5 (WSM5) prognostic variables: snow (q_s), cloud ice (q_i), cloud water (q_c), and mixing ratios of water vapour (q_v) [Federico, 2016]. WSM5 is an updated version of Weather Research Forecast (WRF)-Single-Moment-Microphysics Class 3 (WSM3) by allowing super-cooled water and mixed phase processes. WSM3 is a simple and efficient scheme that consists of snow and ice processes that makes it suitable for mesoscale grid sizes [NOAA Research]. According to the efficiency and theoretical backgrounds of WSM6, it is suitable for both cloud-resolving grids and high-resolution simulations. However, it only anticipates the mass mixing ratios of six water species [Skamarock, 2008]. In WSM6, the number of graupel particles per cubic meter of air: $n_g(D)dD_g(m^{-4})$ follows an exponential size distribution given by:

$$n_g(D)dD_g = n_{og}\exp(-\lambda_g D_g)dD_g \tag{1}$$

where D_g is the graupel diameter, $n_{og}(m^{-4})$ represents the intercept values. $\lambda_g(m^{-1})$ represents the slope of the exponential distribution. This slope is given by:

$$\lambda_g = \left(\frac{\pi n_{og}\rho_g}{\rho q_g}\right)^{\frac{1}{4}} \tag{2}$$

where ρ_g and ρ represents the graupel and air density, respectively. The slope parameter is obtained by multiplying equation (1) by the drop mass ($\frac{\pi\rho_g D_g^3}{6}$) and then integrate by parts three times over all diameters, and finally, the resulting quantities are equated to appropriate water contents (ρq_g). The graupel particle terminal velocity of diameter D_g is given by:

$$V_{Dg} = \alpha_g D_g^{b_g}\left(\frac{\rho_o}{\rho}\right)^{\frac{1}{2}} \tag{3}$$

where α_g represents the empirical formula of the mass weighted speed of graupel (V_g), b_g is the empirical formula of the mass weighted speed of snow V_r, and ρ_o represents the density of air at reference state. According to Rutledge and Hobbs [1984], V_g is obtained by integrating equation (3) and is expressed as:

$$V_g = \frac{\alpha_g\Gamma(4+b_g)}{6}\left(\frac{\rho_o}{\rho}\right)\frac{1}{\lambda_g^{b_g}} \tag{4}$$

where $\Gamma(\gamma)$ is a gamma function. The continuity equation for graupel is given by:

$$\frac{\partial q_g}{\partial t} = -\vec{V}\nabla_3 q_g - \frac{q_g}{\rho}\frac{\partial(\rho V_g)}{\partial z} + S_g \tag{5}$$

where S_g represents the sinks and sources of graupel. $\vec{V}\nabla_3 q_g$ and $\frac{q_g}{\rho}\frac{\partial\rho V_g}{\partial z}$ represent the 3D advection and sedimentation of graupel respectively.

2.2.2 Thompson

Thompson is a bulk microphysical parametrization scheme whose assumed snow size distribution depends on both ice water content and temperature. It consists of number concentration with six classes of moisture species as its prognostic variables: cloud water, graupel, cloud ice, rain, snow, and water vapour [NOAA Research]. Thompson explicitly predicts cloud ice and droplet number concentration due to its inclusion of aerosols as its cloud condensation nuclei (CNN) and ice nuclei (IN). In this scheme, snow size distribution ($N(D)$) is represented by the sum of gamma and exponential distributions, as illustrated in equation (6), and snow assumes a non-spherical shape with a bulk density that varies inversely with its diameter [Skamarock, 2008].

$$N(D) = \frac{M_2^4}{M_3^3} \left[\mathrm{K}_o \exp\left(-\frac{M_2}{M_3}\wedge_o D\right) + \mathrm{K}_1 \left(\frac{M_2}{M_3}D\right)^{\mu_s} \exp\left(-\frac{M_2}{M_3}\wedge_1 D\right) \right] \tag{6}$$

where K_o, K_1, $\wedge_o$ and $\wedge_1$ are snow size distribution constants. μ_s represents the gamma size distribution shape parameter. M_n is the distribution n^{th} moment: $M_n = \int D^n N(D)dD$. M_n allows bulk snow density to be correctly modelled with an inverse diameter dependence in contrast to WSM6 which assumes constant snow density. The first and second term inside the brackets of equation (6) represents the exponential and gamma distributions, respectively. The sum of these two distributions accounts for the general slope of large particles and frequently observed super-exponential number of small particles. Through the use of equation (6) in the scheme enables the effective y intercept parameter to depend on both snow mixing ratios and temperature. The number concentrations (mass mixing ratios) of all forms of water species: vapour, liquid, and solid or aerosol number concentrations follow the same dominant conservation given by:

$$\frac{\partial \Phi}{\partial t} = -\frac{1}{\rho}\nabla \cdot (\rho U \Phi) - \frac{1}{\rho}\frac{\partial(\rho V_\Phi \Phi)}{\partial z} + \delta\Phi + S_\Phi \tag{7}$$

where Φ represents the mass mixing ratio of any water species, U is the 3D wind vector, t is time, V_Φ is the weighted fall speed of Φ, ρ is air density, z is height, $\delta\Phi$ is the sub-grid scale mixing operator, S_Φ is the microphysical process rate terms. The detailed description for newly predicted variables: number of Hygroscopic aerosol (N_{wfa}), number of Non-hygroscopic aerosol (N_{ifa}) i.e., ice-nucleating aerosol and number concentration of cloud droplet (N_c) are provided respectively in equations (8) to (10).

$$\frac{dN_{wfa}}{dt} = -\begin{pmatrix}\text{rain, snow and graupel} \\ \text{collecting aerosols}\end{pmatrix} - \begin{pmatrix}\text{homogeneous nucleated} \\ \text{deliquesced aerosols}\end{pmatrix} - \begin{pmatrix}\text{Cloud Condensation} \\ \text{Nuclei (CCN) activation}\end{pmatrix}$$
$$+ \begin{pmatrix}\text{cloud and rain} \\ \text{evaporation}\end{pmatrix} + (\text{surface emisions}) \tag{8}$$

$$\frac{dN_{ifa}}{dt} = -\begin{pmatrix}\text{rain, snow and graupel} \\ \text{collecting aerosols}\end{pmatrix} - \begin{pmatrix}\text{Ice Nuclei (IN)} \\ \text{activation}\end{pmatrix} + \begin{pmatrix}\text{cloud ice} \\ \text{sublimation}\end{pmatrix} + (\text{surface emissions}) \tag{9}$$

$$\frac{dN_c}{dt} = -\begin{pmatrix}\text{rain, snow and graupel} \\ \text{collecting droplets}\end{pmatrix} - \begin{pmatrix}\text{freezing into} \\ \text{cloud ice}\end{pmatrix} - (\text{ collide into rain}) - (\text{evaporation}) + (\text{CCN activation})$$
$$+ (\text{cloud ice melting}) \tag{10}$$

Thompson assumes that water and ice species follows a generalised gamma distribution defined in equation (11) in instead of the exponential distribution.

$$N(D) = \frac{N_t}{\Gamma(\mu+1)}\lambda^{\mu+1}D^\mu \exp(-\lambda D) \tag{11}$$

where λ represents the slope of the distribution, N_t gives the total number of particles in the distribution, D is the diameter of the particles, and μ is the shape parameter of the distribution. All water and ice species are assumed to use a standard power law form in relating their mass and terminal velocity as a function of diameter. The mass (m(D)) and terminal velocity (V(D)) relations are given by equations (12) and (13) respectively.

$$m(D) = aD^b \tag{12}$$

$$V(D) = \left(\frac{\rho_o}{\rho}\right)^{\frac{1}{2}} \alpha D^\beta \exp(-fD) \tag{13}$$

where a and b are mass power law constants and these vary for different species, f, β, and α are velocity power law constants, ρ_o and ρ are the reference and moist air densities respectively.

3   Data Needs

The meteorological data (Climate Forecast System Reanalysis (CFSR) (ds094)) used for initializing the model to simulate TC Dineo was downloaded from the Research Data Archive (RDA) website [ds0]. CFSR (ds094) dataset was used because TC Dineo occurred between the period of 2011 and 2020. Before downloading the data from RDA website, the period in which TC Dineo occurred was selected starting three days before and ending three days after its occurrence, allowing the model to spin up. On downloading, two datasets, Sea Surface Temperature (SST) and pressure levels, were downloaded from the RDA. SST data sets was extracted for the entire period of occurrence of TC Dineo, i.e., 10th/02/2017 to 20th/02/2017. In contrast pressure levels were extracted for the first six hours of occurrence of TC Dineo, i.e., 13th/02/2017 at 00:00 to 13th/02/2017 at 06:00.

3.1   Model simulation of TC Dineo

The following steps were taken to effect model simulation: (1). We created a run directory which we named case_studies on the Center for high performance computing (CHPC) cluster. (2). Linked the init_atmosphere_model and atmosphere_model executables, physics lookup tables into the case_studies directory. (3). Copied the namelist.*, streams.*, files into the case_studies directory. (4). Downloaded 92km-25km variable resolution mesh (x4.163842.grid.nc) from `https://mpas-dev.github.io`, then push it to the CHPC account in the grid_rotate directory. (5). We used the grid_rotate utility by editing the namelist.input file to set the latitudes and longitudes to the center of interest, then use the grid_rotate utility to rotate the mesh to the new area of refinement (Figure 2), hence producing a new netCDF file used as an input in the streamlist file during static and terrestrial field processing. (6). Push both the downloaded datasets (SST and pressure levels) from the RDA website to the chpc server account into the sst and press directory respectively, run the executable file ungrib.exe to generate intermediate files for both sea surface temperature (SST) and pressure levels. (7). Configured the namelist and the stream files in the init_atmosphere directory, then run the init_atmosphere_model to create initial conditions. (8). Generate idealized initial conditions by interpolating the produced intermediate files with the land surface initial conditions, the created file is used as input in the streams.atmosphere file during model integration.

4   Calibration

4.1   Model configuration and integration

Successful simulations in MPAS depend on how well the prominent microphysics proceses are configured and integrated with the model. The model integration simulation was simulated twice, for WSM6 and Thompson schemes. In the namelist.atmosphere, the &physics section gives as ability to choose our own schemes by changing the namelist variables during model integration. So this gave as chance to perform two simulations i.e., one with WSM6 with other schemes available and Thompson excluded, and finally Thompson with other schemes available and WSM6 excluded. For the case of this study, since we are using 25km variable resolution and we are interested in comparing the capability of WSM6 and Thompson microphysics schemes in simulating TC Dineo over SWIO, we used the mesoscale_reference suit, and override its default after the first simulation.

Mesoscale_reference suit contains WSM6 scheme as its default as shown in table. 1, so for the first simulations with WSM6, we don't adjust anything in the &physics record in the namelist.atmosphere file. For the second simulations, we over-ride the default and change WSM6 to Thompson scheme adding a namlist variable (config_microp_scheme = 'mp_thompson') in the &physics record. This enabled the atmosphere_model to read Thompson scheme during integration instead of WSM6. Before running the atmosphere_model, we first run build_tables executable file to generate lookup tables for the Thompson scheme, since they were not generated initially. This is because the look up tables contain the essential Thompson physics variables necessary for model integration while running with Thompson scheme. Table. 1 illustrates default parameterization and schemes contained in the mesoscale_reference suit which have been tested for mesoscale resolution.

Parameterizations	Schemes
Convection New	Tiedtke
Microphysics	WSM6
Land surface	Noah
Boundary layer	YSU
Surface layer	Monin-Obukhov
Radiation, LW	RRTMG
Radiation, SW	RRTMG
Cloud fraction for radiation	Xu-Randall
Gravity wave drag by orography	YSU

Table 1: Set of parameterization schemes used by mesoscale_reference suit

Having finished configuring the namelist.atmosphere file, the atmosphere_model program produced history and

diagnostic files for the entire period of simulation which were remapped using the convert_mpas utility to produce a netCDF file named latlon.nc which was visualized and used to make analysis.

5 Numerical Experiment Design

The Figure. 2 shows the new transformed mesh, Dineo.grid.nc, to our new area of interest rotated about 90° using the grid_rotate utility.
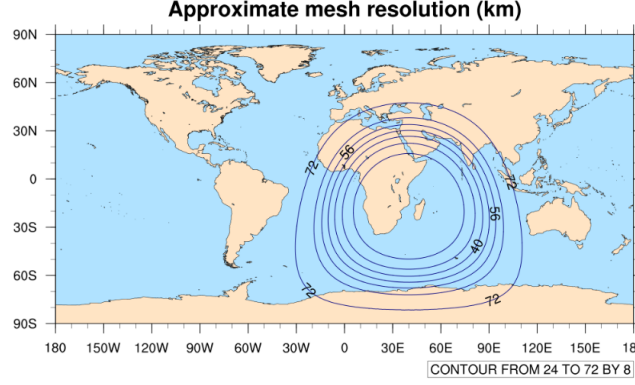

Figure 2: After the grid_rotate

5.1 Detecting and Tracking TC Dineo

After diagnostic and history files were generated during model integration as explained in section 4.1 for the two schemes: WSM6 and Thompson, convert_utility were used to generate a latlon file which contained mean sea level pressure (mslp), zonal wind component (u10), meridional wind component (v10), temperature_250hpa, temperature_500hpa and vorticity_850hpa variables. All these variables were created only for the domain in which TC Dineo occurred, this simplified the tracking because we dealt with a small data set.

The objective measures that we used for detecting and tracking TC Dineo in the tracking algorithm that uses a 6 hourly output data in the latlon file are similar to that described by Kleppek et al. [2008]: (1). The minimum value of mslp over the entire domain termed as the centre of a low pressure system (TC) was determined. (2). $2°$ from the centre of the TC, the warm core which is the average integrated temperature between 250 hpa and 500 hpa was calculated, this core is at least $1°C$ warmer than the surrounding environment which is defined as a $10° \times 10°$ block centred at the mslp. (3). The wind speed which is used to classify the intensity of TC Dineo according to Saffir Simpson scale was calculated using u10 and v10 components over the domain. Then we searched for the maximum value of the wind speed within $5°$ of the cyclone centre. (4). The minimum vorticity within $4°$ of the cyclone centre is determined. Since we are in the SWIO basin, negative vorticity is associated with a cyclone spin.

TC Dineo was detected by comparing the calculated variables above with the cyclone threshold values as follows: (1). The maximum surface wind speed with in $5°$ of the cyclone centre must be greater than $17\,ms^{-1}$. (2). The minimum vorticity must be less than $3.5 \times 10^{-5}\,s^{-1}$. (3). The warm core temperature must be at least $1°C$ greater than the surrounding environment. If the cyclone we identified satisfied the above TC criteria, it was assigned a tracking ID of 1 otherwise 0 for the respective 6 hourly intervals during each day TC Dineo occurred.

The output of the respective computed variables: Date, mslp, latitude, longitude, wind speed, vorticity and warm core temperature with there respective track IDs were visualized for the respective schemes to view the track path of TC Dineo as shown in Figure. 3.

5.2 Track of TC Dineo

As far as we know, the capability of MPAS microphysics schemes (WSM6 and Thompson) in tracking TCs over SWIO has not been investigated yet. Therefore this project also aims at comparing various tracks from four different data sets: reanalysis (red), observation (green), WSM6 (blue), and Thompson (orange) as shown in Figure 3 for the entire lifetime of cyclone Dineo. The small triangles along the trajectories of the various data sets with there respective colours indicate the timing at which TC Dineo matured from being a tropical storm to a category one tropical cyclone.
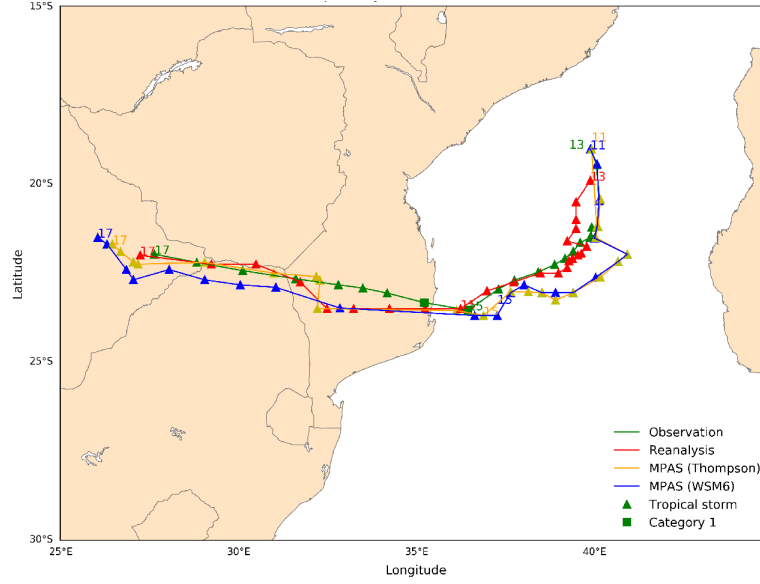
Figure 3: Track of TC Dineo over SWIO depicted by four different datasets (observations, reanalysis, MPAS (Thompson), and MPAS(WSM6)).

On the Figure 3, over water ($19°$-$24°S$; $35°$ - $42°E$), WSM6 and Thompson almost followed the same path as the observation and the reanalysis data, though the tracks started at different time intervals. At around ($35°E$, $23.5°S$), before TC Dineo made landfall over Inhambane (southern Mozambique), it was guided by an easterly steering flow over Mozambique channel induced by a 500 mb high pressure system that prevailed over most southern Africa during the entire lifetime of TC Dineo [Moses and Ramotonto, 2018]. At this location, all the tracks coincided, which means that the simulated data from MPAS, reanalysis and the observation data sets were all consistent in tracing the position of TC Dineo at that location.

From the same Figure 3, it can also be seen that Thompson consistently followed the same track as that of reanalysis over land, which indicated a much better performance than WSM6 in tracking the entire path of TC Dineo. From the Mozambique coast to eastern Botswana, the observation and WSM6 trajectories are positively correlated. However, the track from the simulated data set (WSM6) underestimated the track of TC Dineo as compared to the observation. Over the northern part of South Africa, WSM6 deviated a lot from the three data sets tracks, but all the tracks ended in eastern Botswana. It means that TC Dineo weakened and dissipated in the eastern part of Botswana. It is consistent with observations from Moses and Ramotonto [2018] that TC Dineo weakened to remnant low before hitting Botswana and dissipated on the same day after striking Botswana.

There is a consistency between the spatial distribution (Figure 3) of TC Dineo track and the time evolution of MSLP (Figure 4a). Looking at these two figures all data sets started at different periods and followed different trajectories as TC Dineo dragged southwards, however, on 15th February, all the data sets tracked the cyclone in different locations at different times. Furthermore, all data sets depicted that TC Dineo dissipated in Botswana on the same day (17th February) but in different locations. This is consistent with observations from Moses and Ramotonto [2018].

Generally, both MPAS (Thompson) and MPAS (WSM6) were able to produce a track that resembled the observations, however, Thompson track more closely resembled observations.

Figure 4a shows the time evolution of mean sea level pressure for the entire period of cyclone Dineo for four datasets: ERA5 reanalysis (red), RSMC observation (green), WSM6 (blue), and Thompson (orange). The data was obtained on a six-hourly interval on each TC Dineo occurred. TC Dineo reached its peak on 15th February and this is depicted by both observation and reanalysis data. Both WSM6 and Thompson almost underestimated the day at which TC Dineo matured because they are positively correlated, and their minimum point exits towards the end of 14th. The two MPAS schemes overestimated the peak intensity of MSLP compared to the observation and reanalysis. Looking at the trend of all the data sets, they are all gradually decreasing and then increasing again. This is so because TCs are low pressure systems, therefore during their entire lifetime, the pressure of the eye keeps on dropping until it matures and then increases again, making its sustainable conditions unfavourable hence dissipating as shown in Figure 4a.

Figure 4b illustrates the time evolution of wind speed. All the data set curves are increasing to their maximum and then decrease. This is because when a cyclone is growing, the winds in the eyewall keep on increasing rapidly to the maximum as the cyclone matures. On 14th at around 18:00 tending to 15th, WSM6 and Thompson had their maximum wind speeds, which implies that the storm matured by then, which is consistent with the results in Figure 4a, because at that same time is when WSM6 and Thompson had the lowest values of pressure. The observation data curve reached category 1, but the rest of other data sets remained in the tropical storm region. This implies that both MPAS schemes underestimated the peak intensity of WSPD in comparison with the observation data set. This is may be due to terrain settings during model initialization which affected the magnitude of the wind speed for the two schemes.

Both in Figure 4a and 4b, the observation reached category one on the same day (15th February) and dropped back to tropical storm on the same day, however, the rest of the data sets remained tropical storms during the entire period which is consistent in both figures. This depicts a strong inverse relationship between MSLP and WSPD.

Figure 4c shows the wind pressure relationship. The plot illustrates that the data sets are well correlated to each other, and it depicts a strong relationship between WSPD and MSLP for all the data sets which is consistent with Figure 4a and 4b. This is because the trend in the two curves is opposite to each other, furthermore, the pressure in the eye is always very low, and the eyewall's wind speed is always at maximum. This relationship affected by several factors: TC size, latitude, environmental pressure and the intensification trend. For all the data sets there is a high concentration of the scatter points between 980-1010 hPa, this is because as the cyclone dragged southwards, the latitude kept on decreasing which decreased the Coriolis force, therefore requiring a lesser pressure gradient force to counter balance the tangential wind. The WSM6, Thompson and reanalysis data distributions are almost all coinciding, this means that these data sets follow the same trend.

Figure 4d shows the time evolution of the total precipitation for the entire lifetime of TC Dineo, which formed on 11th February 2017. The total precipitation which is the sum of the accumulated convective and grid scale precipitation is obtained from four data sets. For the first five days, all the data sets almost produced the same total rainfall, however starting on 15th when TC Dineo reached its peak, the following days, the amount of rainfall that was produced was severe. WSM6 produced much rainfall on 16th at around mid day followed by Thompson, then reanalysis and finally the observation data set. Between 13th at 18:00 to 15th at around noon, WSM6 and Thompson are positively correlated. Moses and Ramotonto [2018] claimed that the maximum observed rainfall (mm) recorded on 16th by 12 stations was 17 mm, on 17th was 270 mm by 66 stations and on 18th was 55.5 mm from 49 stations. This claim is consistent with predictions produced by WSM6. Generally, WSM6 simulated the total precipitation better than Thompson, even though both schemes over estimated the total rainfall in comparison with the observation data from 15th till when TC Dineo dissipated (17th).
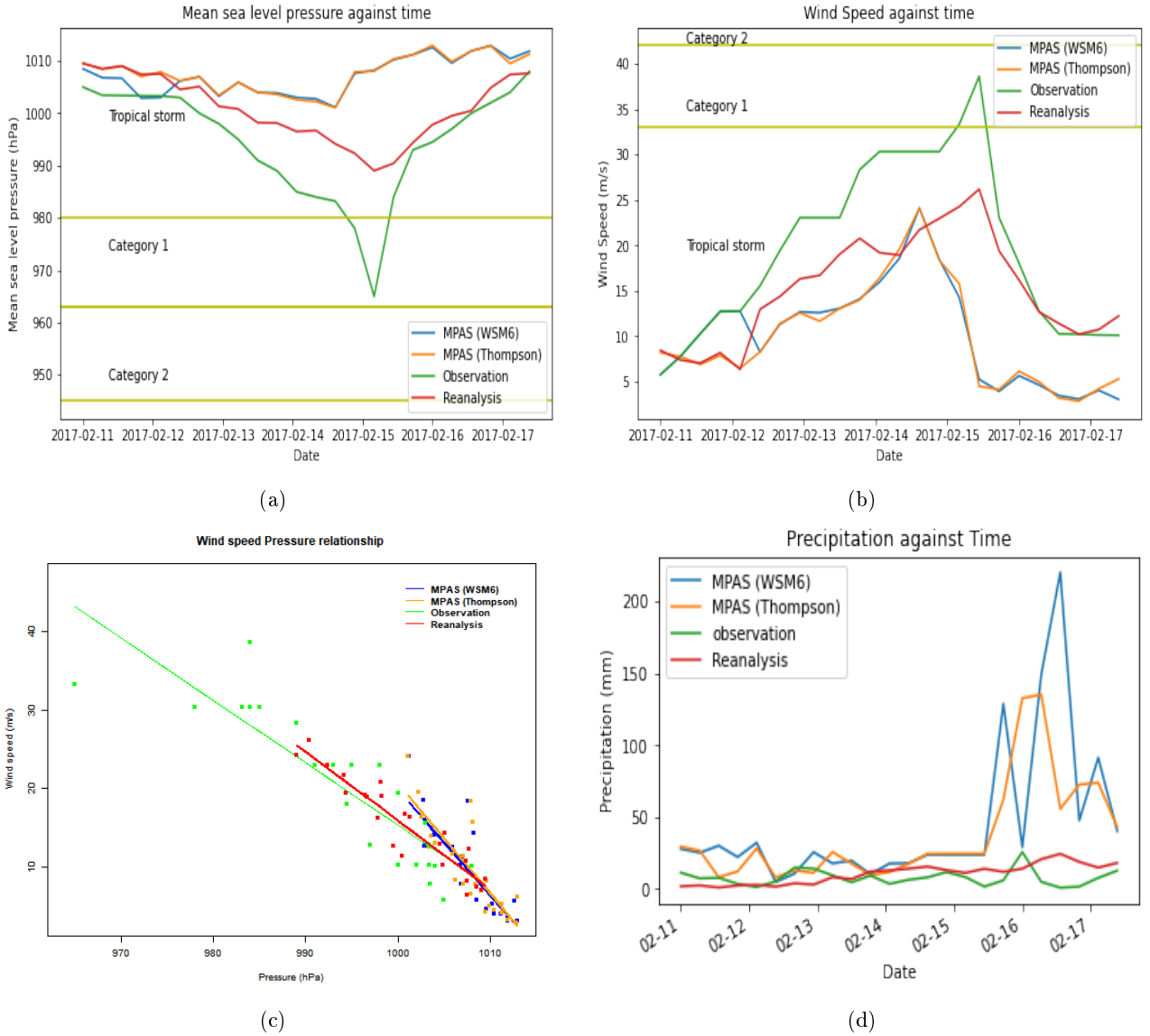

(a)

(b)

(c)

(d)

Figure 4: Time evolution of mean sea level pressure (MSLP), wind speed (WSPD), and Precipitation simulated by reanalysis, observation, Thompson, and WSM6 are depicted by (a), (b), and (d) respectively. (c) depicts the wind speed pressure relationship for the four data sets.

5.3 Horizontal structure of TC Dineo

This section presents the horizontal structure of TC Dineo on 15th February 2017 (day when TC Dineo matured) for WSPD and MSLP obtained from three data sets: Reanalysis, MPAS (Thompson) and MPAS (WSM6).

Figures 5a, 5b and 5c illustrates the horizontal structure for the wind speed for the peak date of TC Dineo. The figures show a cyclonic flow around the eye (almost enclosed by the dark red region) with a high concentration in the east (dark red region) compared to the west. This is due to the converging of the cyclonic flow, the background flow in the eastern region and opposition of the background flow by the cyclonic flow in the western region as the cyclone drags southwards. This is depicted by the vector fields overlaid on the structures. In comparison to the reanalysis structure, both Thompson and WSM6 underestimated the location of the TC Dineo on reaching its peak. The reanalysis structure depicts that the cyclone was just away to make landfall over Inhambane with a maximum wind speed of 26.19 m/s. However, both Thompson and WSM6 simulated that TC Dineo was still a distance away from the coast, even though the maximum wind speed simulated by Thompson (24.17 m/s) is greater than of WSM6 (24.10 m/s). The eyewall (red dark region around the eye) for reanalysis structure is much thicker than that of both Thompson and WSM6 however Thompson's eyewall is thicker than that of WSM6, hence there is a negligible difference between Thompson and WSM6 in simulating the horizontal structure of the wind speed.
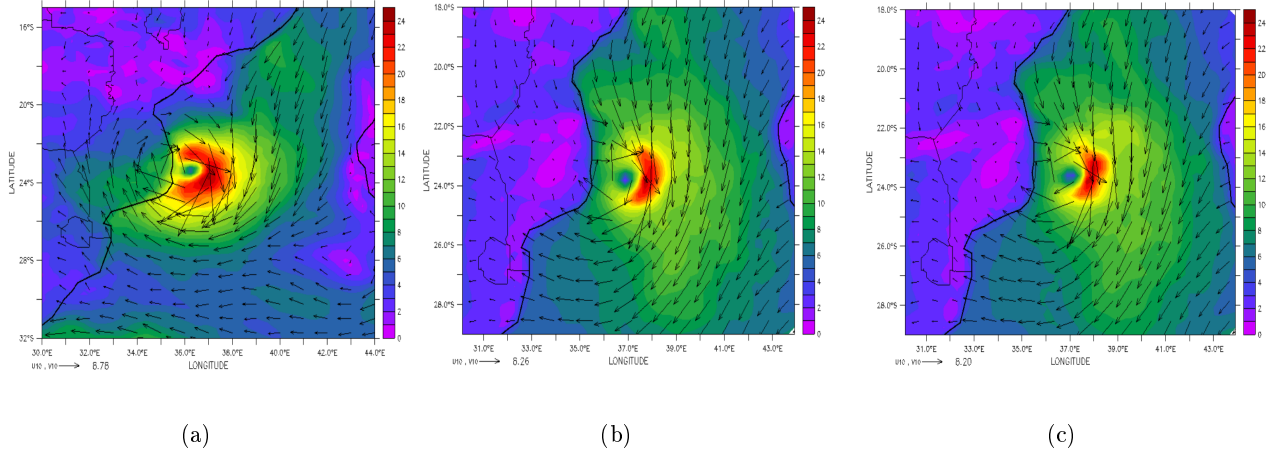

(a) (b) (c)

Figure 5: Horizontal structure of the wind speed (WSPD) for TC Dineo on its peak day (15th Febraury 2017) for three data sets. (a) : Reanalysis, (b) : MPAS (Thompson), (c) : MPAS (WSM6).

Figures 6a, 6b and 6c represents the horizontal distribution of the MSLP in the eye (central purple colour) for three datasets: reanalysis, Thompson, and WSM6 for the peak date of TC Dineo. All the structures were able to predict the lowest pressure centre (eye). The eye in reanalysis is at a pressure of 98900 Pa, and 100200 Pa for both Thompson and WSM6. This implies that both simulated data sets: Thompson and WSM6 overestimated the minimum sea-level pressure. The position of the eye away from the coast is much shorter for reanalysis compared to Thompson and WSM6 even though Thompson is much at a closer distance compared WSM6. These results are consistent with results obtained in figures 5a, 5b, and 5c for the WSPD. The horizontal ascending increase of the MSLP from the eye to other parts of the cyclone is observed in all the figures, consistent with Roy and Kovordányi [2012] literature on the anatomy of TCs.
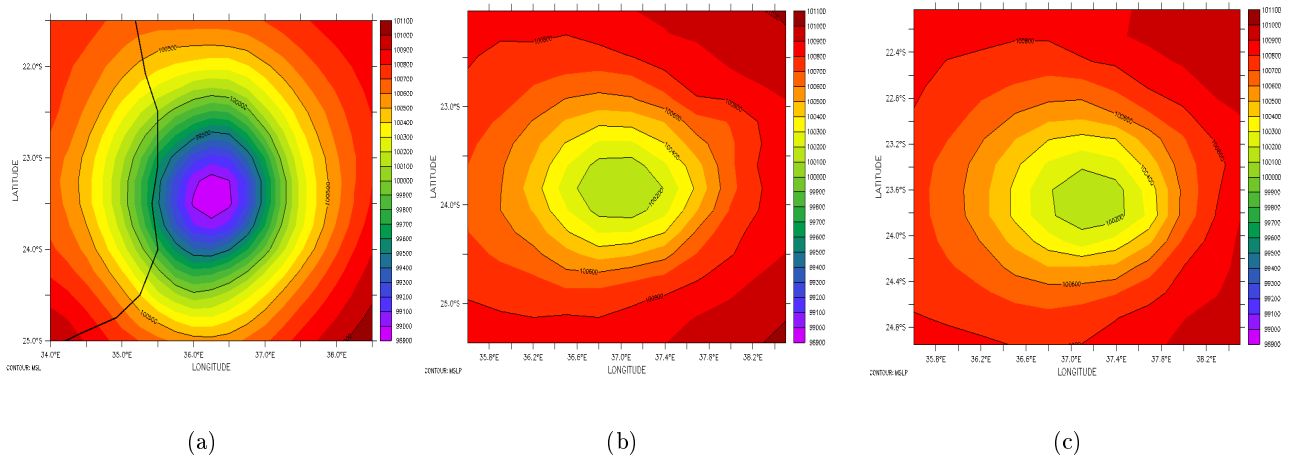

(a) (b) (c)

Figure 6: Horizontal structure of the mean sea level pressure (MSLP) for TC Dineo on its peak day (15th Febraury 2017) for three data sets. (a) : Reanalysis, (b) : MPAS (Thompson), (c) : MPAS (WSM6).

5.4 Vertical cross section of TC Dineo

In this section, the vertical distribution of vorticity, warm core and WSPD on the day when TC Dineo reached its peak are discussed for three data sets: reanalysis, MPAS (Thompson) and MPAS (WSM6).

Based on the fact that TCs are warm core systems, Figures 7a, 7b, and 7c illustrate the vertical structure of temperature of TC Dineo for three datasets. The adiabatic (compressional warming) heat releases of subsiding air causes the eye to be a warm core temperature. This is depicted in all temperature distributions for the three data sets however, it can be seen that it is realistic in the reanalysis distribution compared to that in Thompson and WSM6. In all distributions, warmer temperatures (dark red) in the upper levels and lower in the lower levels are exhibited, this is consistent with the literature about the characteristics of the eye [Roy and Kovordányi, 2012] hence all data sets were able to simulate temperatures of TC Dineo aloft. However the distributions in Thompson and WSM6 slightly differ from that in reanalysis, this means that Thompson and WSM6 exhibited a skill in simulating the temperature structure of TC Dineo.
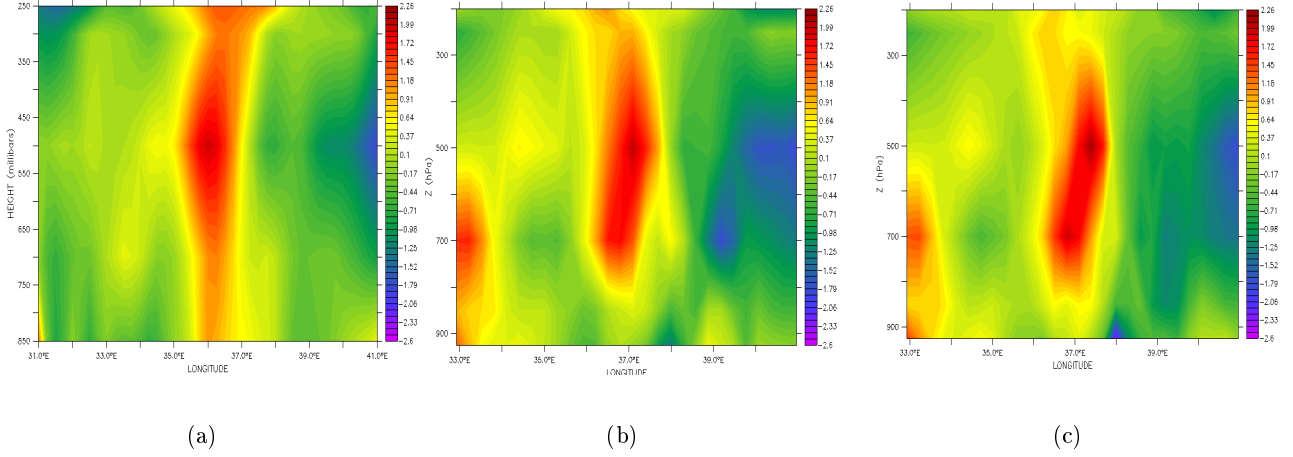

| (a) | (b) | (c) |

Figure 7: Vertical structure of the warm core temperature for TC Dineo on its peak day (15th Febraury 2017) for three data sets. (a) : Reanalysis, (b) : MPAS (Thompson), (c) : MPAS (WSM6).

Figures 8a, 8b, and 8c show the vertical distribution of relative vorticity of TC Dineo on the 15th for three data sets. In all the distributions, relative vorticity in the centre of TC Dineo was well simulated with large negative values at lower levels that slowly increase to smaller values at upper levels. However, the feature is exhibited more in reanalysis and Thompson distributions compared to WSM6. Since TC Dineo formed in the southern hemisphere, negative low-level vorticity is associated with the spinning of a cyclonic rotating cyclone. Reanalysis show a wider area ≈ 1° of large values of negative vorticity compared Thompson and WSM6 at lower levels. However, Thompson ≈ 0.5° predicted a bigger value compared to WSM6 ≈ 0.2°, hence Thompson simulated surface convergence better than WSM6, which is a condition favorable for a cyclone to be sustained. This is consistent with the intercontinental convergence zone (ITCZ) because large negative values cause surface convergence of easterly waves in the southern hemisphere. In all the relative vorticity distributions for all data sets, large areas (red) with positive values of vorticity depict the Southern Indian high pressure system regions [Abiodun, 2016]. Therefore such regions with positive vorticity are associated with subsidence, which often constrains convective precipitation.
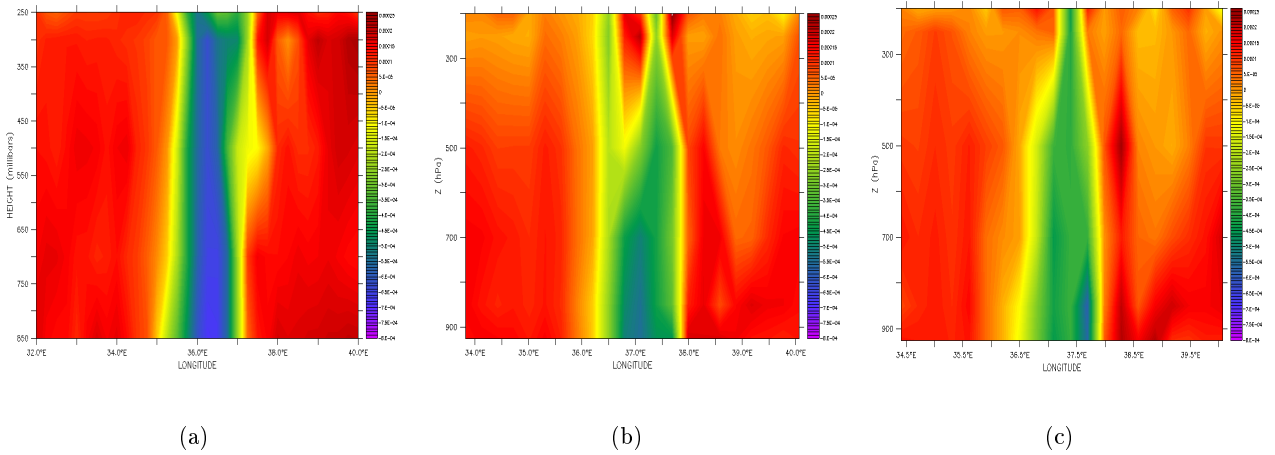

| (a) | (b) | (c) |

Figure 8: Vertical structure of Vorticity for TC Dineo on its peak day (15th Febraury 2017) for three data sets. (a) : Reanalysis, (b) : MPAS (Thompson), (c) : MPAS (WSM6).

References

B. Abiodun. Simulating the characteristics of tropical cyclones over the south west indian ocean using a stretched-grid global climate model. 2016. URL `https://www.ecmwf.int/node/16707`.

Atmospheric physics. Mpas-atmosphere model user's guide. www2.mmm.ucar.edu , `https://www2.mmm.ucar.edu/projects/mpas/mpas_atmosphere_users_guide_7.0.pdf`, Accessed April 2020.

Cyclone Dineo. (2020, 3 15). Cyclone_dineo. En.wikipedia.org, `https://en.wikipedia.org/wiki/Cyclone_Dineo`, Accessed April 2020.

S. Doocy, A. Daniels, C. Packer, A. Dick, and T. D. Kirsch. The human impact of earthquakes: a historical review of events 1980-2009 and systematic literature review. *PLoS currents*, 5, 2013.

S. Federico. Implementation of the wsm5 and wsm6 single moment microphysics scheme into the rams model: verification for the hymex-sop1. *Advances in Meteorology*, 2016, 2016.

L. M. Harris and S.-J. Lin. Global-to-regional nested grid climate simulations in the gfdl high resolution atmospheric model. *Journal of climate*, 27(13):4890–4910, 2014.

A. Hashimoto, J. M. Done, L. D. Fowler, and C. L. Bruyère. Tropical cyclone activity in nested regional and global grid-refined simulations. *Climate Dynamics*, 47(1-2):497–508, 2016.

S. Kleppek, V. Muccione, C. Raible, D. Bresch, P. Köllner-Heck, T. Stocker, C. Muccione, D. Raible, P. Bresch, T. Koellner-Heck, and Stocker. Tropical cyclones in era-40: A detection and tracking method. *Geophys. Res. Lett*, 35, 01 2008.

O. Moses and S. Ramotonto. Assessing forecasting models on prediction of the tropical cyclone dineo and the associated rainfall over botswana. *Weather and climate extremes*, 21:102–109, 2018.

ncar.ucar.edu. (n.d.). Model_for_predicition_across_scales. wikipedia, `https://en.m.wikipedia.org/wiki/Model_for_Predicition_Across_Scales`, Accessed April 2020.

NOAA Research. Wrf namelist.input file description. National Oceanic & Atmospheric Administration , `https://esrl.noaa.gov/gsd/wrfportal/namelist_input_options.html`, Accessed April 2020.

C. Roy and R. Kovordányi. Tropical cyclone track forecasting techniques-a review. *Atmospheric research*, 104:40–69, 2012.

S. Rutledge and P. Hobbs. The mesoscale and microscale structure and organization of clouds and precipitation in midlatitude cyclones. xii: A diagnostic modeling study of precipitation development in narrow cold-frontal rainbands. *Journal of The Atmospheric Sciences - J ATMOS SCI*, 41:2949–2972, 10 1984. doi: 10.1175/1520-0469(1984)041<2949: TMAMSA>2.0.CO;2.

e. a. Skamarock. A description of the advanced research wrf version 3, 2008. NCAR TECHNICAL NOTE.

TROPICAL CYCLONES. Technical hazard sheet - natural disaster profiles. World Health Organization, `https://www.who.int/hac/techguidance/ems/tropical_cyclones/en/`, Accessed April 2020.

Tropical cyclones in the South West Indian Ocean. Tropical cyclones in the south west indian ocean. ReliefWeb, `https://reliefweb.int/report/world/tropical-cyclones-south-west-indian-ocean-new-insights`, Accessed April 2020.

ucar, n.d. mpas_atmosphere_users_guide_6.0. Www2.mmm.ucar.edu, n.d., `https://www2.mmm.ucar.edu/projects/mpas/mpas_atmosphere_users_guide_6.0.pdf`, Accessed April 2020.